RSC Advances

PAPER

View Article Online
View Journal | View Issue

Cite this: *RSC Adv.*, 2020, **10**, 16917

High Eu^{3+} concentration quenching in Y_3TaO_7 solid solution for orange-reddish emission in photonics†

Fernanda Hediger Borges,[a] Fábio José Caixeta,[a] Rafael Ramiro Pereira,[a] Silvana Ruella de Oliveira,[a] Rute A. S. Ferreira[b] and Rogéria Rocha Gonçalves*[a]

We report the synthesis of a Y_3TaO_7 solid solution containing a high Eu^{3+} concentration (from 7 up to 50 mol%) and investigate how Eu^{3+} influences the Y_3TaO_7 crystallization process. To this end, we evaluate the Y_3TaO_7 structural features and photoluminescence properties after Eu^{3+} introduction into the Y_3TaO_7 lattice. The higher the Eu^{3+} ion concentration, the more stable the crystallization process of the Y_3TaO_7 phase seems to be. The Eu^{3+}-containing Y_3TaO_7 displays intense orange-reddish, broad band emission because Eu^{3+} occupies different symmetry sites in the host and causes inhomogeneous broadening. Eu^{3+} emission quenching due to Eu^{3+} concentration is negligible up to 30 mol% and absolute quantum yield values of up to nearly 30% were obtained, making Eu^{3+}-containing Y_3TaO_7 interesting materials for application as high-intensity emitters in photonics.

Received 28th February 2020
Accepted 20th April 2020

DOI: 10.1039/d0ra01912g

rsc.li/rsc-advances

1. Introduction

Inorganic materials have been extensively used as rare earth ion (RE^{3+}) hosts. In particular, metal oxide (M_xO_y) matrixes have been largely employed for this purpose because they present tunable structures, are chemically and thermally stable, exhibit optical transparency over a wide spectral range (UV-NIR), and have a high refractive index and low phonon energy, which all enable their large-scale application in photonics.[1–3] One of the challenges in photonics is the development of materials that allow the incorporation of a high concentration of RE^{3+}, avoiding rare earth cluster formation. The high solubility of RE^{3+} into the host, prevents effective concentration quenching process. As a consequence, these materials can exhibit high emission brightness and intensity, which are requirements for applications in lighting, displays, bioimaging, among others. In this sense, there is a crescent aim to synthesized new promising crystalline structures with great potential of the luminescent properties, which favors RE ion solubility granting a homogeneous distribution of the dopant into the host lattice.

Emphasis have been given to fluorite (CaF_2)-related crystal structures as RE ion hosts.[4–15] The fluorite cubic structure has a general composition of MO_2 per unit cell, where M is a tetravalent metal. Compounds derived from the fluorite structure have aroused growing interest: several materials can be synthesized by replacing the M^{4+} cations with ions of different valences. This substitution generates oxygen vacancies for charge compensation.[9,16–18]

Compounds with the general formula $A_2M_2O_7$ (A = RE and M = Ti, Sn, Zr, Hf) are a class of oxides with fluorite-related structures.[19] Depending on the ratio between the A^{3+} and M^{4+} ionic radii (r_A/r_M), the compound generally crystallizes in fluorite (lower ratio) or pyrochlore crystal structure (higher ratio).[20] In the latter structure, M^{4+} and A^{3+} are coordinated with six and eight oxygen atoms, respectively.[21] Substitution introduces two oxygen vacancies for charge compensation. Pyrochlore and weberite (another kind of crystal structure with the same stoichiometry as pyrochlore) are anion-deficient fluorite-related superstructures.[17] Only a few recent works about fluorite-related structures doped with high RE ion concentrations have been published.[22,23]

Ternary RE ion compounds (RE_3MO_7) are also fluorite-related structures that are closely related to the weberite structure, but replacement is different. The four M^{4+} ions of the fluorite unit cell are replaced with three RE^{3+} ions and one M^{5+} ion (M = Nb, Ta, Sb, Ru, Ir, Os, Re, *etc.*), and one oxygen vacancy arises per fluorite cell.[8,17] Significant differences between the RE^{3+} and M^{5+} ionic radii lead to cation ordering at the metal sites and to oxygen vacancy ordering at the anion sites.[8,10] This structure exhibits distinct RE^{3+} configuration—seven and eight coordination ions, where REO_7 exist between MO_6–REO_8 layers.[17] Depending on RE^{3+} and M^{5+}, the structure and space group in which RE_3MO_7 compounds crystallize vary, and many polymorphic modifications can be obtained only on the basis of processing conditions.[24] The magnetic properties of fluorite-based materials have been studied to a large extent, and their

[a]*Laboratório de Materiais Luminescentes Micro e Nanoestruturados – Mater Lumen, Departamento de Química, FFCLRP, Universidade de São Paulo, SP, Brazil. E-mail: rrgoncalves@ffclrp.usp.br*

[b]*Phantom-G, CICECO-Aveiro Institute of Materials, Department of Physics, University of Aveiro, Aveiro, Portugal*

† Electronic supplementary information (ESI) available. See DOI: 10.1039/d0ra01912g

high versatility has been demonstrated through their application in different areas.[7,8,25–28]

Some structural studies on RE^{3+}-doped fluorite-related structures have shown that RE^{3+} ions are considerably soluble in their hosts. Besides the zirconates and hafnates cited above, there have been reports on tantalates, niobates, and antimonates with high RE^{3+} dopant ion concentration.[9,11,16] Similar ionic radii and valence mean that the RE^{3+} dopant ions preferentially substitute the RE ions of the oxide structure.[29] These complex structures provides a spatial arrangement where the distance between two Eu^{3+} ions allows a higher accommodation of these ions into the lattice without lead to concentration quenching, differently than other oxides.[9] These characteristics make this type of structure interesting for application as high-intensity emitters in photonics.

Fu *et al.*[30] reported that the Y_3TaO_7 crystalline phase consists of an orthorhombic *Ccmm* space group with unit cell parameters related to the fluorite-type cubic structure ($a_{\text{cubic fluorite}} = 5.3$ Å); the relation is $a = 2a_c$, $b = \sqrt{2}a_c$, and $c = \sqrt{2}a_c$ for the Y_3TaO_7 crystalline structure. In this structure, Y^{3+} coordinates with seven or eight oxygen atoms, whereas Ta^{5+} coordinates with six oxygen atoms. Molchanov *et al.*[31] described that Y_3TaO_7 starts to decompose at high annealing temperatures (above 900 °C) and precipitates as Ta_2O_5, which reacts with the former compound to give a polymorphic crystalline phase M′-$YTaO_4$. According to our previous report,[32] at lower Eu^{3+} concentrations (up to 5.0 mol%), Eu^{3+} ions incorporated into the host delay $YTaO_4$ formation.

Introduction of impurities, such as dopant ions, into a crystalline host, is an effective method to manipulate and to control the properties of a material, including its crystalline structure, phase transition, and grain size and shape, among others. The choice of dopant ion is based on similarities between the dopant and the host ions, like the ionic radius, valence, and chemical properties.[33] The dopant ion can occupy either a substitutional or an interstitial site in the host lattice.[34,35] The dopant may be either partially soluble or co-soluble in the host lattice, forming a solid solution and stabilizing a crystalline phase. Therefore, the properties of the solid solution can be tailored for specific applications. In this sense, Eu^{3+} doping into the Y_3TaO_7 lattice can be used not only to study the photoluminescence properties of the resulting solid but also to manipulate the crystalline structure. This is desirable because a pure yttrium tantalate phase is difficult to obtain, due to its polymorphism properties.[36,37]

In this paper, we explore Eu^{3+} solubility within Y_3TaO_7. We discuss how the incorporation of higher Eu^{3+} concentrations into Y_3TaO_7 affects host stabilization and luminescence features. First, we synthesize Eu^{3+}-doped Y_3TaO_7 solid solutions with higher Eu^{3+} concentration (from 7 up to 50 mol%) to investigate how Eu^{3+} influences Y_3TaO_7 crystallization. Next, we evaluate the Y_3TaO_7 structural features after Eu^{3+} is introduced into the lattice and assess the matrix photoluminescence properties, with Eu^{3+} functioning as a structural local-probe. We will show that the matrix excited state lifetime only decreases at the highest Eu^{3+} concentration employed herein. Rising Eu^{3+} concentrations elicit negligible Eu^{3+} emission quenching, which makes the application of these materials as high-intensity emitters in photonics especially interesting.

2. Experimental procedure

2.1 Eu^{3+}-doped Y_3TaO_7 synthesis

Y_3TaO_7 doped with higher Eu^{3+} concentration (from 7 to 50 mol%) was prepared by the sol–gel methodology. Tantalum ethoxide (Sigma-Aldrich, 99.98%), $Y(NO_3)_3$ (Sigma-Aldrich, 99.8%), and $Eu(NO_3)_3$ ethanolic solution were used as precursors. The $Eu(NO_3)_3$ stock solution was prepared from dissolving Eu_2O_3 in HNO_3 aqueous solution, followed by drying at 80 °C and addition of anhydrous ethanol. This solution concentration was carefully confirmed by complexometric titration with EDTA using xylenol orange as an indicator at pH 5.8. The reaction was carried out by basic catalysis with NH_4OH 0.56 mol L^{-1} (Cinética, 24.5%). The reaction mixture was stirred for 1 h, and the resulting solid was separated by centrifugation. Part of the solid was annealed at 900 °C, whereas the other part of the solid was annealed at 1100 °C, for 2 h. The Eu^{3+} quantity in each sample was related to the Y and Ta molar total amount and ranged from 7 to 50 mol%. Samples were labeled SX, with $X = 7$, 10, 15, 20, 30 and 50 mol%. A detailed description of sample preparation can be found elsewhere.[32]

2.2 Characterization

Powder X-ray diffraction (XRD) measurements were obtained on a Siemens-Bruker D5005-AXS diffractometer. The equipment operates with CuKα radiation, $\lambda = 1.5418$ Å, and has a graphite monochromator. Diffractograms were recorded at 0.02° s^{-1} for 2θ values ranging from 5.00 to 90.00°. Diffuse Reflectance Spectroscopy (DRS) was performed between 250 and 600 nm, at room temperature, on a Varian Cary 500 Scan spectrophotometer equipped with a Harrick Co Praying Mantis diffuse reflection accessory. Fourier transform infrared (FT-IR) spectroscopy spectra were measured on a PerkinElmer FTIR Spectrum Two instrument spectrometer in the 4000–400 cm^{-1} range, with a resolution of 2 cm^{-1}. Powder samples were mixed with KBr pellets. Photoluminescence steady-state spectra were recorded on a Fluorolog-3 Horiba Scientific (model FL3-22) spectrofluorometer equipped with a FL1073 Horiba photomultiplier and the excitation source used was a 450 W Xe arc lamp. Time-resolved measurements were carried out in a Horiba Jobin Yvon Triax 550 Fluorolog spectrofluorometer, the xenon lamp pulsed mode and a Spex DM302 photomultiplier were employed. Emission decay curves were recorded on a Fluorolog 3 Horiba Scientific (model FL3-22) equipped with a Hamamatsu R928 photomultiplier with xenon lamp pulsed mode. The absolute emission quantum yield values (q) were measured at room temperature using a C9920-02 Hamamatsu system. The method is accurate within 10%.

3. Results and discussion

3.1 Structural and vibrational properties

Fig. 1 shows the X-ray diffractograms of the Eu^{3+}-doped samples annealed at 900 or 1100 °C. All crystalline planes correspond to

the Y_3TaO_7 phase (JCPDS 01-071-1346 48-265), a fluorite-related orthorhombic structure with space group *Ccmm*[30,38] and unit cell parameters $a = 10.486$, $b = 7.426$, and $c = 7.448$ Å. Six oxygen atoms surround tantalum, in an octahedral arrangement; yttrium atoms are coordinated with seven or eight oxygen atoms. The tantalum and yttrium atoms are organized as a deformed cube with missing oxygen and as a slightly deformed cube, respectively.[30]

Previously it was demonstrated that rising Eu^{3+} content up to 5.0 mol% leads to a secondary monoclinic crystalline phase named M′-$YTaO_4$ (JCPDS 24-1425) with space group $P12/a1$, which is also verified for the non-doped host.[32] The Eu^{3+} concentration of 7.0 mol% (sample S7) stabilizes Y_3TaO_7, and the secondary phase is absent. No significantly intense peaks related to Eu^{3+}-based oxides or secondary crystalline phases appear even in the presence of higher Eu^{3+} concentration in the host, which indicates that Eu^{3+} ions are homogeneously distributed in the lattice, resulting in a solid solution, indicating that Y_3TaO_7 provides high RE ion solubility. The diffractogram of S15 and S30 annealed at 1100 °C display negligible low-intense diffraction peaks corresponding to the M′-$YTaO_4$ phase, as observed by baseline magnification presented at the right side of Fig. 1. Therefore, this phase is considered as an impurity. The diffraction patterns observed for the samples afford only for the mentioned crystalline phases. No further peaks attributed to RE oxides were detected.

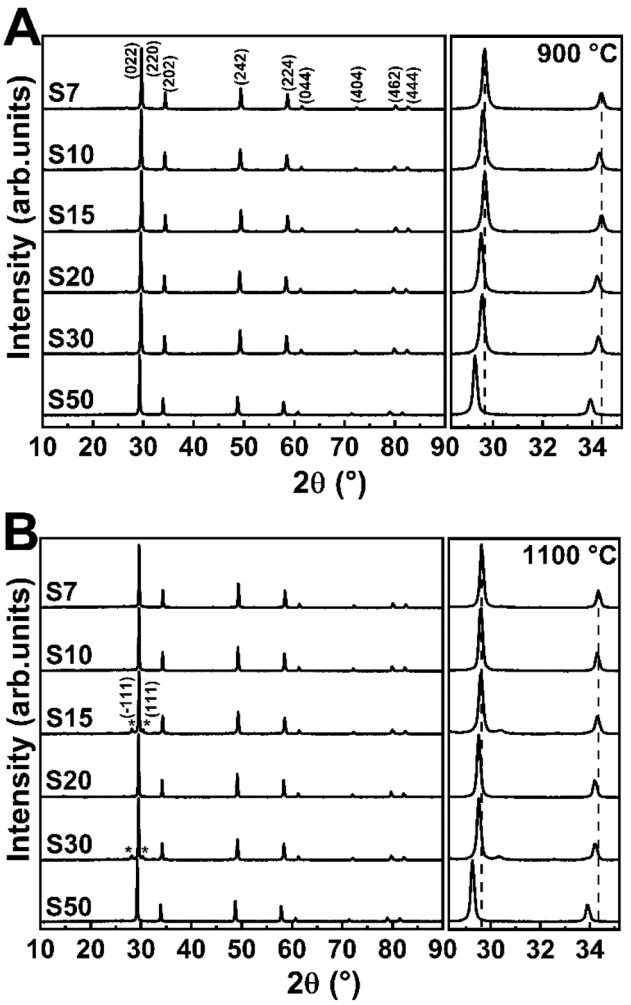

Fig. 1 X-ray diffractograms of Eu^{3+}-doped Y_3TaO_7 samples annealed at (A) 900 or (B) 1100 °C for 2 h. The M′-YTaO4 phase planes are marked (*). At the right side, a magnification in the region of 28–35° and 2θ shift is observed.

An expanded view of the diffractograms in the 2θ range of 28–35° can be observed in Fig. 1, where the most intense diffraction peaks appear for the Eu^{3+}-doped Y_3TaO_7 samples annealed at 900 or 1100 °C. All the diffraction peaks shift to lower 2θ values at higher Eu^{3+} concentration. In agreement with Bragg's law, it indicates increasing interplanar spacing (d) in the Y_3TaO_7 crystalline structure. Higher interplanar spacing is due to the slightly larger Eu^{3+} ionic radius (1.066 Å) as compared to the ionic radius of the Y^{3+} ions (1.019 Å) that Eu^{3+} substitutes.[39] Peak shifts toward lower angles confirm that a substitutional homogeneous solid solution $(Y\text{-}Eu)_3TaO_7$ emerges. The slight difference between the Eu^{3+} and Y^{3+} ionic radii culminates in mismatched sizes, so substitution of Y^{3+} for Eu^{3+} causes a slight lattice expansion.

We reported that Eu^{3+} incorporation into the Y_3TaO_7 host affects crystallization and delays formation of M′-$YTaO_4$ as a secondary crystalline phase as compared to the undoped sample.[32] M′-$YTaO_4$ formation is pronounced up to a Eu^{3+} concentration of 5.0 mol% because Y_3TaO_7 decomposes and reacts with precipitated Ta_2O_5, to generate $YTaO_4$.[31] However, Eu^{3+} concentrations higher than 5.0 mol% induce Y_3TaO_7 phase stabilization because a solid solution arises. Y_3TaO_7 no longer decomposes, so $YTaO_4$ is absent. The solid solution probably originates in a specific range of Eu^{3+} concentrations higher than 5.0 mol%.

As discussed before, Y_3TaO_7 contains two different Y^{3+} coordination sites in the unit cell: one-third of the Y^{3+} ions are octacoordinated, whereas two-thirds are heptacoordinated. Hinatsu *et al.*[40] recently reported substitution in LnY_2TaO_7 for a series of lanthanides. When larger ions substitute Y^{3+}, they preferentially occupy the octacoordinated position, whilst smaller ions tend to engage in heptacoordination. Therefore, unit cell parameters for Ln = Eu^{3+} are $a = 10.5287$, $b = 7.4554$, and $c = 7.4926$ Å;[40] *i.e.*, unit cell dimensions increase due to the presence of larger Eu^{3+} ions in the host.

Fig. 2A, B and Table 1 display the bandgap energy determined by using the absorption coefficients (estimated by the reflectance data and the Kubelka–Munk equation[41] – Fig. S1 and S2, ESI†) and the Tauc plot[42] for direct bandgap. Minor bandgap energy changes were detected, namely, from 4.76 to 4.86 eV for the samples annealed at 900 °C and from 4.71 to 4.85 eV for the samples annealed at 1100 °C. Only the samples S50 at both annealing temperatures showed lower values of band gap (4.54 and 4.66), which agrees with the observed in the XRD analysis. The literature reports a bandgap of 4.6 eV for Y_3TaO_7 (ref. 43) and a higher bandgap value for the resulting solid solution. We notice that the Eu^{3+} incorporation into the host lattice affects the bandgap energy. For samples S7–S50, their close band gap energy values show that a similar structure; *i.e.*, stabilized $(Y\text{-}Eu)_3TaO_7$ solid solution. As already discussed for lower Eu^{3+}

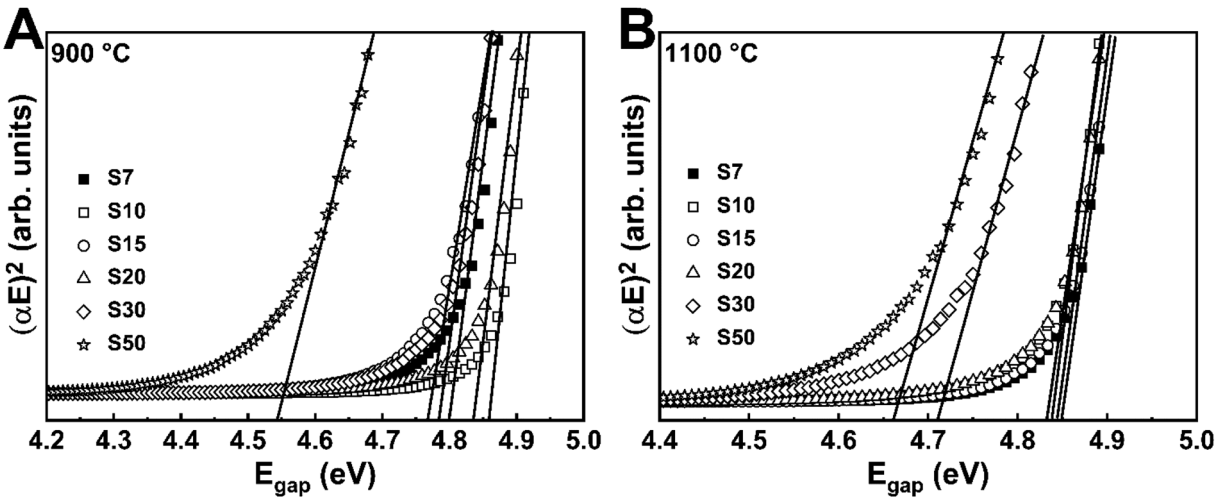

Fig. 2 Tauc plot of Eu^{3+}-doped Y_3TaO_7 annealed at (A) 900 °C and (B) 1100 °C.

Table 1 Optical band gap energy values obtained from the Tauc plot for the Eu^{3+}-doped Y_3TaO_7 samples annealed at 900 or 1100 °C

	Host absorption (±0.01 eV)	
Sample	900 °C	1100 °C
S7	4.79	4.85
S10	4.86	4.83
S15	4.76	4.84
S20	4.83	4.83
S30	4.78	4.71
S50	4.54	4.66

concentrations, these samples have high transparency in the UV range, and there is no luminescence quenching due to host absorption.

The Eu^{3+}-doped Y_3TaO_7 samples without annealing and annealed at 900 or 1100 °C were analyzed by FTIR (Fig. S3†). After annealing, the spectra indicate full removal of water and organic substances, which could decrease luminescence and quantum emission efficiency by the non-radiative process through excited-state deactivation. The higher frequency band is around 820 cm^{-1} (Ta–O–Ta stretching vibration[44]), highlighting that Y_3TaO_7 has relatively low phonon energy.

3.2 Luminescent properties

Fig. 3 depicts the excitation spectra of samples S7–S50 annealed at 900 or 1100 °C, monitored through the Eu^{3+} $^7F_0 \rightarrow {}^5D_2$ transition at 607.0 nm. A broadband with more than one contribution in the UV region, centered at around 270 nm, emerges in all the spectra. It corresponds to charge transfer (CT) from an O^{2-} (2p) partially filled shell to a Eu^{3+} (4f) filled shell and from the tantalate group, which is associated with the charge transfer between O^{2-} to Ta^{5+}.[45,46] Moreover, the other contribution is associated with the host absorption. As observed previously, the energy gap values are approximately 4.8 eV (from 251 to 254 nm), which also corresponds to the range of the observed broadband and indicates the energy transfer from host lattice to Eu^{3+} excited states.[47,48] Also, sharp peaks above 350 nm are characteristic of Eu^{3+} f–f transitions. The bands at 360, 394, 415, 462, and 529 nm are assigned to transitions from the ground state $^7F_{0,1}$ to $^5D_4$, $^5L_6$, $^5D_3$, $^5D_2$, and $^5D_1$, respectively. These spectral profiles are very similar to the spectral profiles of pure Y_3TaO_7 and of Y_3TaO_7 with lower Eu^{3+} concentrations (0.1 and 0.5 mol%).[32]

We recorded the emission spectra of Eu^{3+}-doped Y_3TaO_7 samples annealed at 900 or 1100 °C (Fig. 4) under excitation at the CT band (~275 nm). The emission spectra under excitation at the Eu^{3+} f–f transitions at 394 ($^7F_0 \rightarrow {}^5L_6$) and 464 nm ($^7F_0 \rightarrow {}^5D_2$) are depicted in Fig. S4.† These spectra contain mostly broad bands centered at 578, 590–595, 605–633, 653, and 710 nm, which refer to $^5D_0 \rightarrow {}^7F_J$ ($J = 0$, 1, 2, 3, and 4), respectively.

The samples annealed at 900 °C have emission spectra with very broadbands (full-width-at-half-maximum of, fwhm, ~9 nm), independently of the selected excitation wavelengths, as already noticed.[32] The Y_3TaO_7 crystalline structure contains two possible coordination sites for Y^{3+} ions; *i.e.*, hepta- and octa-coordination. Eu^{3+} probably replaces Y^{3+} in the two different symmetry sites and is randomly distributed. In these spectra, Eu^{3+} occupies the same average symmetry site. The broad (fwhm ~ 70 cm^{-1}) $^5D_0 \rightarrow {}^7F_0$ transition detected in all the spectra suggests that Eu^{3+} occupies more than one symmetry site (without inversion center in accordance with the higher relative intensity of the $^5D_0 \rightarrow {}^7F_2$ transition). The fact that the samples annealed at 900 °C display a similar spectral profile indicates high correspondence in terms of Eu^{3+} distribution in similar local-coordination symmetry sites. Eu^{3+}-doped fluorite-related compounds with pyrochlore structure, such as rare-earth zirconates, hafnates, niobates, and tantalates, exhibit a similar spectral profile with analogous broad bands.[11,22,23,49–51]

The samples annealed at 1100 °C have slightly different spectra even in the presence of the same crystalline phase, as discussed previously. Concerning broadening, the samples

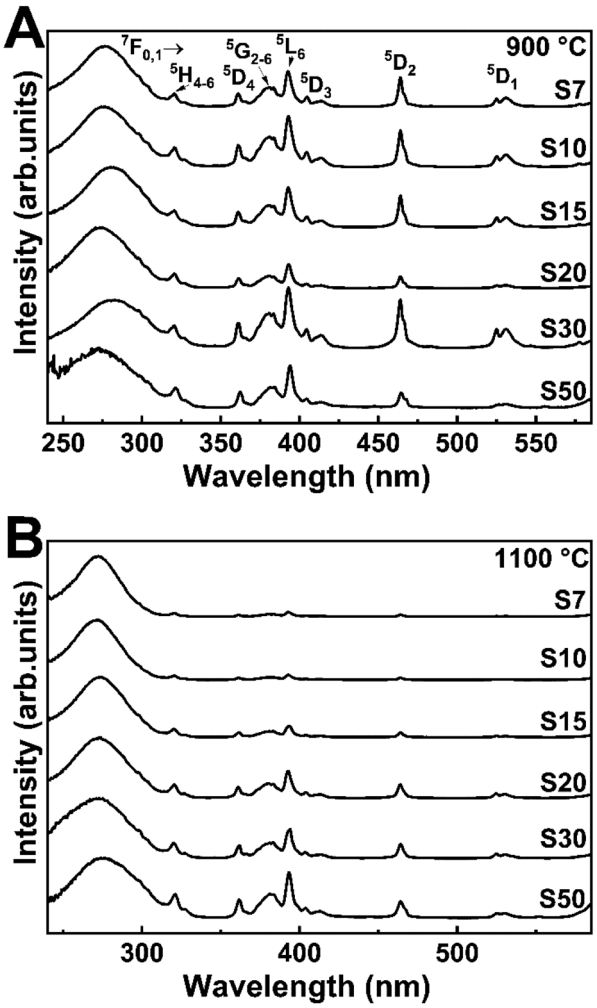

Fig. 3 Excitation spectra at fixed emission wavelength of 607.0 nm of the Eu^{3+}-doped Y_3TaO_7 samples annealed at (A) 900 and (B) 1100 °C.

annealed at 1100 °C clearly have the same pattern as the samples annealed at 900 °C. Depending on the excitation wavelength, a sharper peak at 611.5 nm stands out. When this sharper peak occurs more evidently, the $^5D_0 \rightarrow {}^7F_0$ transition tends to disappear. This different emission profile resembles the Eu^{3+} emission profile in M′-$RETaO_4$.[32,52] In conclusion, most of the Eu^{3+} ions are occupying Y_3TaO_7 symmetry sites. However, as the temperature increases, and M′-$YTaO_4$ is minimally formed, Eu^{3+} tends to occupy M′-$YTaO_4$ symmetry; that is, Eu^{3+} substitutes Y^{3+} in a C_2 site.[47,53] Although this secondary phase is not evident in the XRD analysis, the photoluminescence spectra clearly indicate the formation of a distinct phase for the samples annealed at 1100 °C.

Table S1† shows the $^5D_0 \rightarrow {}^7F_2/{}^5D_0 \rightarrow {}^7F_1$ intensity ratios, calculated from the respective area of each transition, fitted by Lorentzian functions, for all the Eu^{3+} doping concentrations and sample annealing temperatures. The samples annealed at 1100 °C have lower $^5D_0 \rightarrow {}^7F_2/{}^5D_0 \rightarrow {}^7F_1$ ratios than the samples annealed at 900 °C mainly because fewer structural defects exist at higher annealing temperature, as discussed based on bandgap energy measurements. In general, Eu^{3+} occupies slightly higher symmetry sites in the samples annealed at 1100 °C. However, the difference between the samples is not significant, suggesting that Eu^{3+} is still in the same average symmetry sites.

Besides, it is also important to take the presence of Eu^{3+} in a different symmetry site into account for the samples S15 and S30 annealed at 1100 °C. The spectral profile of Eu^{3+} in Y_3TaO_7 symmetry sites can be seen for these samples in a magnified view and it will be discussed later. The more intense $^5D_0 \rightarrow {}^7F_2$ transition band at 611.5 nm corresponds to Eu^{3+} occupying M′-$YTaO_4$ sites.

In order to demonstrate the occupation of Eu^{3+} ions in two different symmetry sites of Y_3TaO_7 and M′-$YTaO_4$ hosts, Fig. 5 shows the emission spectra for S15 at 1100 °C under different excitation wavelengths. Although the S15 sample annealed at 900 °C shows the crystallization of a single-phase, its emission spectrum was used as a reference to estimate the Eu^{3+} in Y_3TaO_7 emission of the sample annealed at 1100 °C. In Fig. 5 it is possible to observe the change in the S15 at 1100 °C sample spectral profile at different excitation wavelengths. The gray patterned area in each spectrum corresponds to the normalized

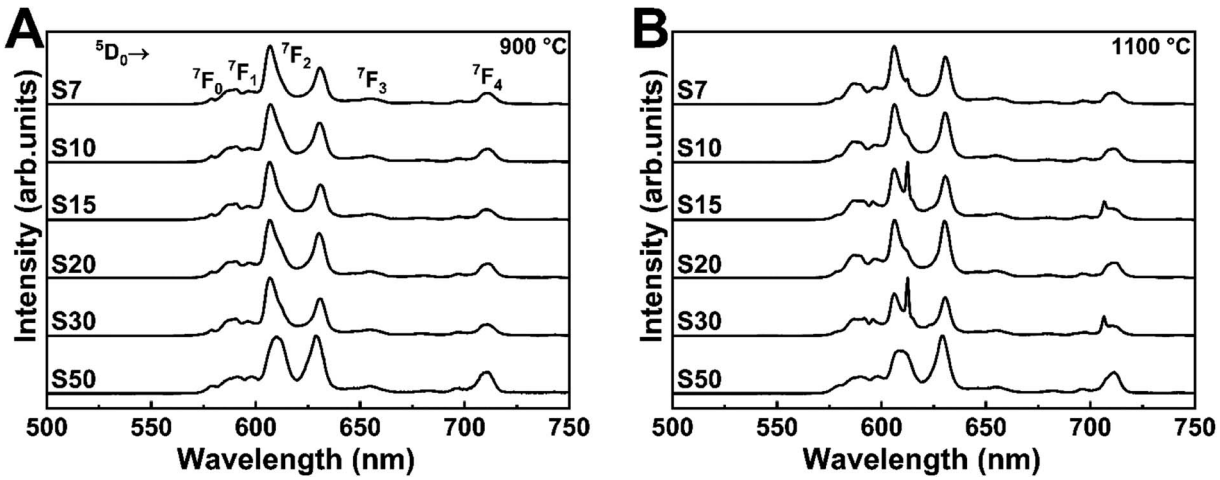

Fig. 4 Emission spectra under excitation at CTB (~275 nm) of Eu^{3+}-doped Y_3TaO_7 samples annealed at (A) 900 or (B) 1100 °C.

spectrum of S15 at 900 °C, which has a pure Y_3TaO_7 phase and then multiplied by the indicated factor to adjust under the obtained spectra of S15 at 1100 °C. For this estimate, all spectra were normalized.

Under CT band excitation, at 275.0 nm, Eu^{3+} ions that are distributed into Y_3TaO_7 lattice are preferentially activated. The contribution of the band that corresponds to $YTaO_4$ CT band is smaller at this excitation wavelength. Under excitation at 393.0 nm, the major contribution comes from the Eu^{3+} in M′-$YTaO_4$ symmetry site, providing a sharper spectrum, even though the Eu^{3+} in Y_3TaO_7 is also present. Even for a small amount of the secondary phase, Eu^{3+} ions into M′-$YTaO_4$ host is evident. For all these spectra in Fig. 5, both Eu^{3+} ions into Y_3TaO_7 and M′-$YTaO_4$ were activated.

In Fig. 6, we tried to show the two different symmetry sites that appear in sample S15 annealed at 1100 °C separately.

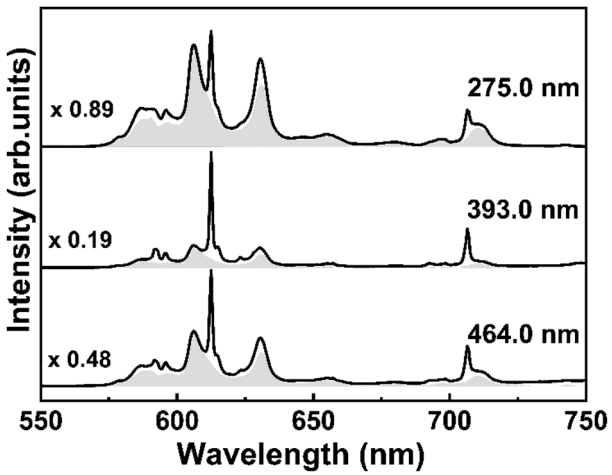

Fig. 5 Emission spectra under different excitation wavelengths and submitted to a mathematic manipulation to show the contribution of the different symmetry sites present in the sample S15 annealed at 1100 °C.

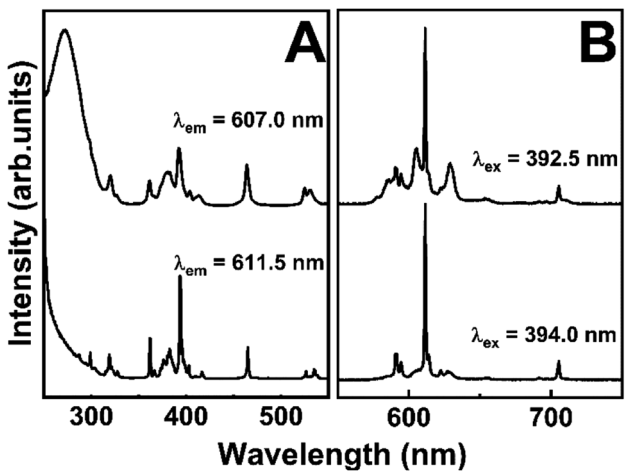

Fig. 6 (A) Excitation spectra with emission fixed at 607.0 and 611.5 nm. (B) Emission spectra upon excitation at 392.5 and 394.0 nm.

Fig. 6A shows the excitation spectra with fixed emission at two different wavelengths (607.0 and 611.5 nm), evidencing that the bands observed for $^5D_0 \rightarrow {}^7F_2$ transition come from different symmetry sites. Eu^{3+} ions into Y_3TaO_7 lattice provides the large spectral profile and Eu^{3+} into M′-$YTaO_4$ host, results in sharper spectra. In Fig. 6B, under 394.0 nm excitation, it is possible to activate almost only the Eu^{3+} into M′-$YTaO_4$, with C_2 symmetry.[47] Under 392.5 nm excitation, Eu^{3+} ions in both hosts are activated. Even performing a time-resolved emission measurement under 392.5 nm excitation (Fig. S5†), it was not possible to distinguish different symmetry site besides the diminish of the peak referent to Eu^{3+} into M′-$YTaO_4$, at 611.5 nm, which possess lower lifetime than Eu^{3+} ions into Y_3TaO_7.

Fig. 7 contains the $^5D_0$ excited state emission decay curves for all the Eu^{3+}-doped Y_3TaO_7 samples annealed at 900 or 1100 °C under excitation at CT band with emission at 607 nm (the curves under excitation at 393 and 464 nm are presented in Fig. S6, ESI†). The samples display an almost single exponential behavior and have been fitted by using a first-order exponential. This indicates that even Eu^{3+} ions exist in different symmetry sites, the lifetime values are close to each other. We obtained τ_1 lifetimes values from decay curves for each sample under different excitation wavelengths (see Table 3).

Samples with higher Eu^{3+} concentration (S7–S50) behave in the same way as samples doped with lower Eu^{3+} concentration (0.1 up to 5.0 mol%). The samples annealed at 1100 °C have higher $\tau_{1/e}$ values, which refer to greater elimination of species (like OH groups) that deactivate the Eu^{3+} excite state. We already observed that Eu^{3+}-doped Y_3TaO_7 has a long lifetime (about 1.80 ms for the sample containing Eu^{3+} at 0.5 mol%, annealed at 1100 °C).[32] The lifetime of samples with higher Eu^{3+} concentration (S7–S50) that have stabilized Y_3TaO_7 crystalline phase is longer than that of the samples with lower concentration (up to 5 mol%).

Analysis of these samples under the same excitation wavelength and with Eu^{3+} concentration higher than 20 mol% shows that these samples have reduced $\tau_{1/e}$. Although the S30 and S50 samples exhibit strong luminescence, the lifetime values suggest quenching by concentration: a shorter Eu^{3+} ion – Eu^{3+} ion distance promotes energy transfer. Energy migration combined with host defects explains such quenching.

For the samples annealed at 1100 °C that exhibited the sharp peak at 611.5 nm (Fig. 4B, S4B and D†), we measured the lifetime of both peaks that are assigned to $^5D_0 \rightarrow {}^7F_2$ transition, the large one at $\lambda_{em} = 607.0$ nm (as can be seen in Fig. 7 and Table 2) and the sharp one at $\lambda_{em} = 611.5$ nm. The decay curves of these samples for this last-mentioned wavelength were adjusted with the non-single exponential fit, that was not reported here, and the $\tau_{1/e}$ values are exhibited in Table 3. Lower $\tau_{1/e}$ values were obtained under excitation at 393.0 and 464.0 nm with emission fixed at 611.5 nm than the values obtained with the emission at 607.0 nm.

The shorter lifetime values may be related to increasing Eu^{3+} content to structural changes ($Y_3TaO_7 \rightarrow$ M′-$YTaO_4$) because Eu^{3+} in the latter phase has a shorter lifetime.[32] Eu^{3+} ions that occupy symmetry sites in this structure have a shorter lifetime

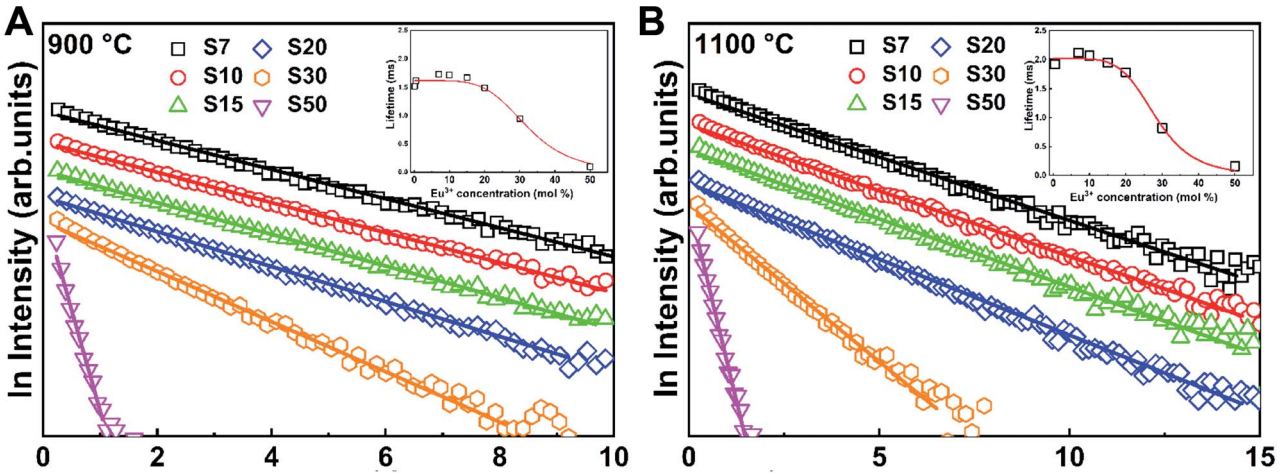

Fig. 7 PL decay curves for curves for the Eu^{3+} $^5D_0$ excited state under excitation at CTB of Eu^{3+} doped Y_3TaO_7 samples annealed at (A) 900 or (B) 1100 °C with fixed emission at 607.0 nm. Inset: lifetime values (τ_{obs}) as a function of Eu^{3+} concentration (from 0.1 [30] up to 50 mol%) under excitation at CTB. The lines are visual guides.

Table 2 $^5D_0$ excited state lifetimes (±0.01 ms) for Eu^{3+}-doped Y_3TaO_7 samples annealed at 900 or 1100 °C under different excitation wavelengths

Annealing temperature (°C)	Sample	CTB	393.0 nm	464.0 nm
900	S7	1.74	1.68	1.59
	S10	1.75	1.73	1.66
	S15	1.68	1.48	1.52
	S20	1.54	1.53	1.52
	S30	1.00	1.01	1.00
	S50	0.13	0.12	0.12
1100	S7	2.18	2.14	2.00
	S10	2.16	2.10	2.02
	S15	2.08	1.96	1.96
	S20	1.87	1.81	1.81
	S30	0.86	0.96	0.90
	S50	0.17	0.18	0.19

and lower symmetry (C_2). Photoluminescent measurements and lifetime decay curves of most of the samples annealed at 1100 °C have shown the presence of the M′-$YTaO_4$ crystalline phase, which had not been detected in the XRD diffractograms. The lifetime values of the samples showed in Table 3 are similar to those values of samples doped with 1, 2, and 5 mol% of Eu^{3+} concentration.[32]

Table 3 $^5D_0$ excited state lifetimes (ms) for Eu^{3+}-doped yttrium tantalate samples annealed at 1100 °C with emission fixed at 611.5 nm and under excitation at 393.0 and 464.0 nm

	$\tau_{1/e}$ (±0.01 ms)	
Samples	393.0 nm	464.0 nm
S7	1.42	1.41
S10	1.41	1.48
S15	1.26	1.31
S20	—	1.41
S30	0.70	0.80

In order to observe the quenching effect as a function of Eu^{3+} concentration, Fig. S7† brings $\tau_{1/e}$ values for each sample, measured with emission fixed at 607.0 nm for the $^5D_0 \rightarrow {}^7F_2$ transition, for evaluation in the Y_3TaO_7 host. Samples S10 and S7 have a longer lifetime, for samples annealed at 900 °C and 1100 °C, respectively. Although lifetime decreases slightly from S7 to S20, their $\tau_{1/e}$ values are close. Samples S30 and S50 have significantly lower lifetime values, indicating that quenching due to concentration takes place. The lifetime dependence on the excitation wavelength is another argument supporting distinct local-coordination sites. Also, the presence of CTB intermediate state in near-resonance with the $^5D_0$ emitting level mediating energy transfer is known to induce a lifetime increases relative to its intrinsic or natural lifetime measured under direct intra-$4f^6$ excitation (393.0 and 464.0 nm).[54]

It is possible to describe the behavior of the $^5D_0$ excited state lifetime values decreases as a function of Eu^{3+} ions concentration from the following equation:[55,56]

$$\tau_{obs} = \frac{\tau_0}{1 + (r/Q)^p} \quad (1)$$

where τ_{obs} is the experimental lifetime value, τ_0 is the radiative lifetime (ideal), r is Eu^{3+} ions concentration, Q is the quenching concentration and p is the phenomenological parameter that gives curve profile. The graphs inserted in Fig. 7 show the dependence of $^5D_0$ lifetime as a function of Eu^{3+} ions concentration up to 50 mol% of Eu^{3+} under excitation at CTB (the graphs referent to excitation at 393 and 464 nm excitation are shown in Fig. S8†). The lifetime values of the samples doped with 0.1 and 0.5 mol% [32] were included in this calculus since the Eu^{3+} are in the same symmetry sites of the samples presented in this work.

The best fit obtained from the equation data for each curve is represented by a red line. Therefore, the average calculated parameters were: $\tau_0 = 1.62 \pm 0.01$ ms, $Q = 32$ mol%, and $p = 5$ for the samples annealed at 900 °C and $\tau_0 = 2.01 \pm 0.01$ ms, $Q = 29$ mol%, and $p = 5$ for the samples annealed at 1100 °C.

Table 4 Judd–Ofelt parameters of the Eu^{3+}-doped Y_3TaO_7 samples annealed at 900 or 1100 °C under 394 nm excitation

Annealing temperatures	Samples	Ω_2 (10^{-20} cm^2)	Ω_4 (10^{-20} cm^2)	A_{rad} (s^{-1})	τ_{rad} (ms)	τ_{exp} (ms)
900 °C	S7	7.34	4.03	592	1.69	1.63
	S10	7.63	3.97	606	1.65	1.76
	S15	7.23	3.33	569	1.76	1.43
	S20	7.24	3.97	584	1.71	1.51
	S30	7.40	3.51	583	1.72	0.99
	S50	9.29	4.19	697	1.43	0.13
1100 °C	S7	5.78	2.26	462	2.16	2.14
	S10	6.08	2.40	481	2.08	2.09
	S15	6.57	5.38	587	1.70	1.93
	S15[a]	5.61	2.01	451	2.22	1.26
	S20	5.32	2.13	431	2.32	1.78
	S30	6.69	6.42	620	1.61	0.98
	S50	7.02	3.27	550	1.82	0.19

[a] This values are referent to the emission spectra of Fig. 6B, which represents the Eu^{3+} ions into the M′-$YTaO_4$ sites almost isolated, in contrast to values calculated for Eu^{3+} ions into Y_3TaO_7 lattice.

These yttrium tantalate samples had exhibited a high quenching concentration at about 30 mol% of Eu^{3+} ions, a much higher value than the observed for other materials, such zirconates, hafnates,[22,23] antimonates,[9] for example. The high quenching concentration of Eu^{3+} ions in this host can be attributed to the facility of substitution of these ions in the place of Y^{3+} ions of the host, therefore, the RE^{3+} ions have high solubility in this host due to the similarity of ionic radii.

Judd–Ofelt intensity parameters, radiative (A_{rad}) and non-radiative (A_{nrad}) transition probabilities were calculated based on emission spectra under excitation at 393 nm shown at Fig. S4.† The refractive index used to calculate these parameters was 1.8, estimated by using specular reflectance on a film prepared using the same precursors as the powders, by dip-coating technique.[32] The calculated values were based on the characteristic spectra of Y_3TaO_7 as well as the comparison with the experimental lifetime values, where the emission was fixed at the Y_3TaO_7 $^5D_0 \rightarrow {}^7F_2$ transition (~607 nm). The quantum efficiency values were omitted due the very close values between the τ_{exp} and τ_{rad} calculated. Therefore, the calculated quantum efficiency for some samples showed values higher than 100%. This can be an indicative that the refractive index value used for the calculations do not corresponds to the real value of the samples, affecting the obtained value. The powder annealing can result in a material with less densification, smaller refractive index value and, thus, a higher lifetime value. This behavior can be observed in nanostructured materials. For example, in Y_2O_3:Eu^{3+} samples where the radiative lifetime is 0.9 ms (calculated and measured from a monocrystal), for particulated nanostructured materials, the experimental lifetime value is highly dependent on the annealing temperature. Previous studies showed that lifetime values higher than 0.9 ms, and as the material was annealed at higher temperatures or for longer time, there was a reduction in these lifetime values.[57,58] This fact can explain the higher τ_{exp} found for these yttrium tantalate samples.

Even though, this group of samples has presented higher values of radiative transition probabilities (A_{rad}) and τ_{rad} than the group of samples with lower Eu^{3+} concentration.[32] In the previous work, it was shown that these samples clearly show the presence of M′-$YTaO_4$ phase. To show the influence of Eu^{3+} ions located in this phase on A_{rad} and τ_{rad}, it was calculated these values based on the almost isolated emission spectra of sample S15 annealed at 1100 °C depicted in Fig. 6B (λ_{ex} = 394 nm) and the τ_{exp} presented in Table 4 (λ_{em} = 611.5 nm). The quantum efficiency value calculated for this sample was 57%.

Table 4 lists the experimental Ω_2 and Ω_4 intensity parameter values for all the samples and the refractive index value used was 1.8. The values of sample S15 at 1100 °C marked ([a]) are referent of the same emission spectra referred previously (Fig. 6B).

The samples with higher Eu^{3+} concentration have presented higher Ω_2 than the samples with lower concentration.[32] The environment could become more polarizable and less symmetric, which agrees with the $^5D_0 \rightarrow {}^7F_2/{}^5D_0 \rightarrow {}^7F_1$ asymmetric ratio (Table S1†).

Absolute emission quantum yield was measured and the obtained values are shown in Table 5. Under excitation at CTB (250 and 280 nm), the values were about 10%. For other fluorite-type structure materials, the obtained values were 15–18% for

Table 5 Emission quantum yield values (%) under different excitation wavelengths (250, 280, 320, 393, and 464 nm) of the Eu^{3+}-doped Y_3TaO_7 samples annealed at 900 and 1100 °C. The experimental error is 10%

	900 °C				1100 °C		
λ (nm)	S7	S10	S20	S50	S10	S20	S50
250	7.4	10.0	11.0	—	8.8	11.0	3.9
280	7.1	9.9	9.3	—	7.2	10.0	1.7
320	2.9	4.7	5.3	—	1.9	5.7	1.3
393	—	17.0	11.0	2.5	6.0	14.0	10.0
464	—	29.0	15.0	2.6	16.0	15.0	7.0

$Y_2Hf_2O_7$:5% Eu^{3+},[50] 9.89% for $La_2Hf_2O_7$:5% Eu^{3+},[22] and 17.6% for $La_2Zr_2O_7$:5% Eu^{3+} [23] under 258 nm (CTB) excitation. These values were comparable to the values obtained for the Eu^{3+}-doped Y_3TaO_7 when excited at the same wavelength. For the excitation at 393 and 464 nm (direct excitation at Eu^{3+} ion levels $^5L_6$ and $^5D_2$, respectively), the obtained values were higher, reaching approximately 30% for the S10 sample annealed at 1100 °C, superior than other materials described in literature, such as YAG:16% Eu^{3+}, which shows a quantum yield value of 15.5%.[59]

Fig. 8 shows the Commission Internationale d'Eclairage (CIE) 1931 chromaticity diagram and the values calculated for the (x, y) color coordinates from the emission spectra of the samples under excitation at CTB. The emission color of all Eu^{3+}-doped Y_3TaO_7 samples is reddish-orange.

The orange emission is the strongest in Eu^{3+}-doped rare-earth titanates.[60] Eu^{3+} is located at a centrosymmetric site in compounds with the pyrochlore structure (D_{3d}), so electric dipole transitions are forbidden. The $^5D_0 \rightarrow {}^7F_1$ magnetic dipole transition is the strongest emission in this case, and distortions to the symmetry site can be evaluated by splitting of this transition.[19] The emission of the $^5D_0 \rightarrow {}^7F_1$ transition is orange. For zirconates and hafnates, their structures are distorted in such a way that the electric dipole transitions become stronger. In these structures, the orange emission is stronger when Eu^{3+} is located in sites with an inversion center because the $^5D_0 \rightarrow {}^7F_1$ transition dominates. In distorted lattices, the local symmetry becomes distorted (deviation from the inversion center), and the red emission component dominates.[61]

The symmetry sites are greatly distorted in Y_3NbO_7 (ref. 49 and 62) and Y_3TaO_7. Consequently, these compounds present the $^5D_0 \rightarrow {}^7F_0$ transition and high-relative intensity $^5D_0 \rightarrow {}^7F_2$ transition, so emission is redder. In Eu^{3+}-doped Y_3SbO_7,[9] which belongs to the same space group as Y_3TaO_7, emission goes from reddish-orange to red with increasing Eu^{3+} concentration. It is possible to see that the emission of Eu^{3+} inserted in Y_3TaO_7 host is reddish-orange almost independently of the increasing of Eu^{3+} concentration in this case.

The emission becomes redder depending on the amount of M′-$YTaO_4$ in the structure.[32] The higher the Eu^{3+} concentration, the more stable the Y_3TaO_7 solid solution, so emission color tends to orange. This indicates that the emission of the compounds is tunable, depends on the structure, and can be tailored by the Eu^{3+} concentration in the host.

The purity of the emitted color can be characterized from the equation below:[63,64]

$$\text{Color purity} = \sqrt{\frac{(x_s - x_i)^2 + (y_s - y_i)^2}{(x_d - x_i)^2 + (y_d - y_i)^2}} \times 100 \qquad (2)$$

where (x_s, y_s) are the color coordinates calculated from the emission spectra of each sample, (x_i, y_i) are the coordinates of the white illuminant (0.333, 0.333), and (x_d, y_d) are the coordinates of the dominant wavelength. The coordinates of the dominant wavelength used to this calculation were (0.657, 0.343) for 607 nm, corresponding to $^5D_0 \rightarrow {}^7F_2$ transition. The color purity varied from 95.2–96.3% and 92.6–94.7% for the samples annealed at 900 °C and 1100 °C, respectively, showing the high color purity of this material. These materials can be efficiently excited by UV and blue light generating reddish-orange light, which can be used for several applications such as for lasers, lighting, displays,[65] and the development of warm LEDs.[66] Also, other potential application of the reddish-orange emitters materials is in greenhouses, as artificial light, that can improve the absorption of the chlorophyll of the plants in this region of the spectrum, better than in the green region.[67]

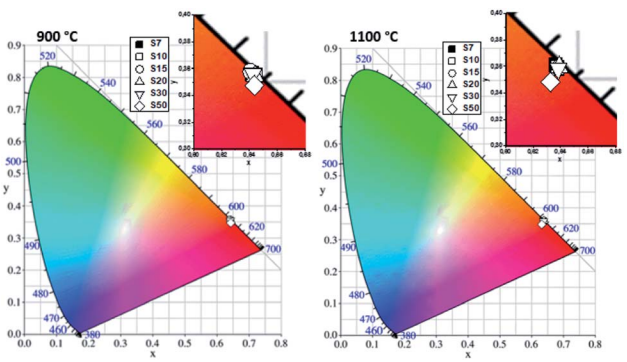

Fig. 8 CIE 1931 chromaticity diagram of Eu^{3+}-doped Y_3TaO_7 samples annealed at (A) 900 or (B) 1100 °C under excitation at CTB.

4. Conclusions

We successfully synthesized Y_3TaO_7 solid solutions containing high Eu^{3+} concentration, from 7 up to 50 mol%. It was evaluated the Y_3TaO_7 structural features after Eu^{3+} introduction into the lattice and also evaluated the photoluminescence properties; Eu^{3+} ions photoluminescence properties functioned as a structural probe. The higher the Eu^{3+} concentration, the more stable the Y_3TaO_7 crystallization. Emission bands were intense ($q \sim$ 30%) and broad (fwhm $\sim$ 9 nm). Inhomogeneous broadening was due to the occupation of Eu^{3+} ions in a different symmetry sites. Eu^{3+} emission quenching due to concentration was negligible for the samples containing up to 30 mol%, and quantum yield values of nearly 30% were obtained with excitation in Eu^{3+} f–f transitions, which makes these materials especially interesting for application as high-intensity emitters in photonics. The results reported here call attention to the design of materials based on the tunability of their emission color through manipulation of their crystalline structure, which can be tailored by controlling the Eu^{3+} quantity in the sample.

Conflicts of interest

There are no conflicts to declare.

Acknowledgements

The authors want to acknowledge Brazilian Funding Agencies FAPESP (grant number 2017/11301-2 and the scholarships processes numbers 2017/10424-3 and 2018/04587-0), CNPq and

CAPES for financial support. This work was also developed within the scope of the project CICECO-Aveiro Institute of Materials, UIDB/50011/2020 & UIDP/50011/2020, financed by national funds through the FCT/MEC and when appropriate co-financed by FEDER under the PT2020 Partnership Agreement. We also would like to thank Mrs Cynthia Maria de Campos Prado Manso for reviewing the text.

References

1 C. N. R. Rao, *Annu. Rev. Phys. Chem.*, 1989, **40**, 291–326.
2 Y. Kanke and A. Navrotsky, *J. Solid State Chem.*, 1998, **141**, 424–436.
3 E. De la Rosa-Cruz, L. A. Diaz-Torres, P. Salas and R. A. Rodriguez, in *Third International Conference on Solid State Lighting*, SPIE, 2004, vol. 5187, p. 150.
4 D. Michel, M. P. y. Jorba and R. Collongues, *J. Raman Spectrosc.*, 1976, **5**, 163–180.
5 S. V. Krivovichev, *Solid State Sci.*, 1999, **1**, 211–219.
6 J. L. Payne, M. G. Tucker and I. R. Evans, *J. Solid State Chem.*, 2013, **205**, 29–34.
7 Y. Doi, Y. Harada and Y. Hinatsu, *J. Solid State Chem.*, 2009, **182**, 709–715.
8 Y. Hinatsu, H. Ebisawa and Y. Doi, *J. Solid State Chem.*, 2009, **182**, 1694–1699.
9 J. Wang, Y. Cheng, Y. Huang, P. Cai, S. Il Kim and H. J. Seo, *J. Mater. Chem. C*, 2014, **2**, 5559–5569.
10 K. P. F. Siqueira, R. M. Borges, E. Granado, L. M. Malard, A. M. De Paula, R. L. Moreira, E. M. Bittar and A. Dias, *J. Solid State Chem.*, 2013, **203**, 326–332.
11 T. Linda Francis, P. Prabhakar Rao, S. K. Mahesh, T. S. Sreena and S. Parvathi Babu, *Opt. Mater.*, 2016, **52**, 134–143.
12 H. J. Rossell, *J. Solid State Chem.*, 1979, **27**, 115–122.
13 H. J. Rossell, *J. Solid State Chem.*, 1979, **27**, 287–292.
14 Y. Hinatsu and Y. Doi, *J. Ceram. Soc. Jpn.*, 2019, **127**, 273–278.
15 A. Egaña, E. Cantelar, M. Tardío and J. E. Muñoz Santiuste, *Opt. Mater.*, 2019, **97**, 109393.
16 L. T. Francis, P. Prabhakar Rao, M. Thomas, S. K. Mahesh, V. R. Reshmi and T. S. Sreena, *Phys. Chem. Chem. Phys.*, 2014, **16**, 17108–17115.
17 L. Cai and J. C. Nino, *Acta Crystallogr., Sect. B: Struct. Sci.*, 2009, **65**, 269–290.
18 K. E. Sickafus, R. W. Grimes, J. A. Valdez, A. Cleave, M. Tang, M. Ishimaru, S. M. Corish, C. R. Stanek and B. P. Uberuaga, *Nat. Mater.*, 2007, **6**, 217–223.
19 R. A. McCauley and F. A. Hummel, *J. Lumin.*, 1973, **6**, 105–115.
20 C. R. Stanek, C. Jiang, B. P. Uberuaga, K. E. Sickafus, A. R. Cleave and R. W. Grimes, *Phys. Rev. B: Condens. Matter Mater. Phys.*, 2009, **80**, 17.
21 M. A. Subramanian, G. Aravamudan and G. V. Subba Rao, *Prog. Solid State Chem.*, 1983, **15**, 55–143.
22 K. Wahid, M. Pokhrel and Y. Mao, *J. Solid State Chem.*, 2017, **245**, 89–97.
23 M. Pokhrel, M. Alcoutlabi and Y. Mao, *J. Alloys Compd.*, 2017, **693**, 719–729.
24 K. P. F. Siqueira, J. C. Soares, E. Granado, E. M. Bittar, A. M. De Paula, R. L. Moreira and A. Dias, *J. Solid State Chem.*, 2014, **209**, 63–68.
25 Y. Hinatsu and Y. Doi, *J. Solid State Chem.*, 2013, **198**, 176–185.
26 M. Wakeshima and Y. Hinatsu, *J. Solid State Chem.*, 2010, **183**, 2681–2688.
27 D. Harada and Y. Hinatsu, *J. Solid State Chem.*, 2001, **158**, 245–253.
28 M. Wakeshima, H. Nishimine and Y. Hinatsu, *J. Phys.: Condens. Matter*, 2004, **16**, 4103–4120.
29 S. Fujihara and K. Tokumo, *Chem. Mater.*, 2005, **17**, 5587–5593.
30 W. T. Fu and D. J. W. IJdo, *J. Solid State Chem.*, 2009, **182**, 2451–2455.
31 V. V. Molchanov, M. G. Zuev, L. M. Plyasova and S. V. Bogdanov, *Inorg. Mater.*, 2004, **40**, 73–79.
32 F. H. Borges, F. J. Caixeta, R. R. Pereira, S. R. de Oliveira and R. R. Gonçalves, *J. Lumin.*, 2018, **199**, 143–153.
33 D. Chen and Y. Wang, *Nanoscale*, 2013, **5**, 4621–4637.
34 E. Setiawati and K. Kawano, *J. Alloys Compd.*, 2008, **451**, 293–296.
35 D. A. Rani, Y. Yoshizawa, K. Hirao and Y. Yamauchi, *J. Am. Ceram. Soc.*, 2004, **87**, 289–292.
36 K. P. F. Siqueira and A. Dias, *Mater. Res.*, 2014, **17**, 167–173.
37 Y. Yokogawa and M. Yoshimura, *J. Am. Ceram. Soc.*, 1991, **74**, 2077–2081.
38 Y. Yokogawa, M. Yoshimura and S. Somiya, *Mater. Res. Bull.*, 1987, **22**, 1449–1456.
39 R. D. Shannon, *Acta Crystallogr., Sect. A: Cryst. Phys., Diffr., Theor. Gen. Crystallogr.*, 1976, **32**, 751–767.
40 Y. Hinatsu and Y. Doi, *J. Solid State Chem.*, 2016, **233**, 37–43.
41 E. M. Patterson, C. E. Shelden and B. H. Stockton, *Appl. Opt.*, 1977, **16**, 729.
42 J. Tauc, R. Grigorovici and A. Vancu, *Phys. Status Solidi*, 1966, **15**, 627–637.
43 R. Abe, M. Higashi, K. Sayama, Y. Abe and H. Sugihara, *J. Phys. Chem. B*, 2006, **7**, 2219–2226.
44 G. Blasse and G. P. M. Van Den Heuvel, *Phys. Status Solidi*, 1973, **19**, 111–117.
45 K. P. F. Siqueira, P. P. Lima, R. A. S. Ferreira, L. D. Carlos, E. M. Bittar, F. M. Matinaga, R. Paniago, K. Krambrock, R. L. Moreira and A. Dias, *J. Phys. Chem. C*, 2015, **119**, 17825–17835.
46 M. Zhao, Z. Zhao, L. Yang, X. Wang, F. Yan and C. Xing, *J. Mater. Sci.: Mater. Electron.*, 2017, **28**, 16008–16012.
47 B. Li, Z. Gu, Y. Dong, J. Lin and M. Su, *Chem. Res. Chin. Univ.*, 1999, **15**, 226–231.
48 G. Blasse and A. Bril, *J. Lumin.*, 1970, **3**, 109–131.
49 K.-Y. Kim, U.-C. Chung, B. Mutulet, F. Weill, A. Demourgues, J. Rossit, J.-M. Heintz, A. Veillere and V. Jubera, *Inorg. Chem.*, 2017, **56**, 4495–4503.
50 M. Pokhrel, K. Wahid and Y. Mao, *J. Phys. Chem. C*, 2016, **120**, 14828–14839.
51 J. Papan, D. J. Jovanović, K. Vuković, K. Smits, V. Đorđević and M. Dramićanin, *Opt. Mater.*, 2016, **61**, 68–76.

52 B. Li, Z. Gu, J. Lin and M. Z. Su, *J. Mater. Sci.*, 2000, **35**, 1139–1143.
53 B. Li, Z. Gu, J. Lin and M. Z. Su, *Mater. Res. Bull.*, 2000, **35**, 1921–1931.
54 R. A. S. Ferreira, M. Nolasco, A. C. Roma, R. L. Longo, O. L. Malta and L. D. Carlos, *Chem.–Eur. J.*, 2012, **18**, 12130–12139.
55 X. Orignac, D. Barbier, X. Min Du, R. M. Almeida, O. McCarthy and E. Yeatman, *Opt. Mater.*, 1999, **12**, 1–18.
56 R. R. Gonçalves, G. Carturan, M. Montagna, M. Ferrari, L. Zampedri, S. Pelli, G. C. Righini, S. J. L. Ribeiro and Y. Messaddeq, in *Optical Materials*, Elsevier, 2004, vol. 25, pp. 131–139.
57 K. De Oliveira Lima, R. Rocha Gonçalves, D. Giaume, A. Ferrier and P. Goldner, *J. Lumin.*, 2015, **168**, 276–282.
58 J. L. Ferrari, M. A. Schiavon, R. R. Gonçalves, A. M. Pires and M. R. Davolos, *Thin Solid Films*, 2012, **524**, 299–303.
59 I. E. Kolesnikov, D. V. Tolstikova, A. V. Kurochkin, A. A. Manshina and M. D. Mikhailov, *Opt. Mater.*, 2014, **37**, 306–310.
60 A. Garbout, N. Kallel Kchaou and M. Férid, *J. Lumin.*, 2016, **169**, 359–366.
61 M. Hirayama, N. Sonoyama, A. Yamada and R. Kanno, *J. Lumin.*, 2008, **128**, 1819–1825.
62 K. Y. Kim, A. Durand, J. M. Heintz, A. Veillere and V. Jubera, *J. Solid State Chem.*, 2016, **235**, 169–174.
63 Y.-F. Wu, Y.-T. Nien, Y.-J. Wang and I.-G. Chen, *J. Am. Ceram. Soc.*, 2012, **95**, 1360–1366.
64 T. S. Sreena, P. P. Rao, A. K. V. Raj and T. R. A. Thara, *J. Alloys Compd.*, 2018, **751**, 148–158.
65 V. Dubey, J. Kaur, S. Agrawal, N. S. Suryanarayana and K. V. R. Murthy, *Superlattices Microstruct.*, 2014, **67**, 156–171.
66 Y. Ren, Y. Liu and R. Yang, *Superlattices Microstruct.*, 2016, **91**, 138–147.
67 Y. Han, F. Song, Q. Li, F. Wang, C. Ming and J. Tian, *Opt. Mater.*, 2014, **37**, 756–759.